DIRECT ANALYTICAL EFFICIENCY ASSESSMENT OF THE NaI(Tl) GAMMA-RAY DETECTOR (*ROMASHKA*)

by

Abouzeid A. THABET [1,2]***, Mohamed S. BADAWI*** [3,4*]***, Ayman HAMZAWY*** [5]***,***
Ivan N. RUSKOV [6,7]***, Mohamed I. BADAWI*** [1]***, Ivan A. SIRAKOV*** [7]***,***
Yuri N. KOPATCH [6]***, Dimitar N. GROZDANOV*** [6,7]***, and Bohaysa A. SALEM*** [8]

[1] Department of Biomedical Equipment Technology,
Faculty of Applied Health Sciences Technology, Pharos University, Alexandria, Egypt
[2] Department of Educational Studies, University of Technology and Applied Sciences, Khasab, Oman
[3] Physics Department, Faculty of Science, Alexandria University, Alexandria, Egypt
[4] Faculty of Sciences, Alamein International University, Alamein City, Matrouh Governorate, Egypt
[5] College of Pharmacy, Al-Farahidi University, Baghdad, Iraq
[6] Frank Laboratory of Neutron Physics, Joint Institute for Nuclear Research, Dubna, Russia
[7] Institute for Nuclear Research and Nuclear Energy, Bulgarian Academy of Sciences, Sofia, Bulgaria
[8] Basic Science Department, Faculty of Physical Therapy, Pharos University in Alexandria, Egypt

Scientific paper
https://doi.org/10.2298/NTRP2501022T

The present study focuses on the analytical and numerical calculations of the solid angle, effective solid angle, efficiency, and gamma-ray average path length within the detector materials as a function of the source position. This analysis is conducted for a *Romashka* module of the 4π NaI(Tl) gamma-ray detector array (NaGRaDA). NaGRaDA comprises 2 × 2π gamma-ray detector modules, with each module consisting of six NaI(Tl) crystals arranged in a compact configuration resembling a *Daisy* flower (known as *Romashka* in Russian). Each of the twelve scintillators has a unique design, distinguishing them in shape and size from conventional scintillation detectors. This type of 4π multi-detector system is applicable for measuring gamma radiation from samples exhibiting very low activity. It is employed in neutron activation analysis and prompt-gamma neutron activation analysis. Furthermore, this system can be instrumental in the experimental investigation of the characteristics of neutron-induced nuclear reactions. The results obtained throuh direct analytical and numerical methods will be compared with the upcoming comprehensive characterization of the upgraded and modernized *Romashka* NaGRaDA. This comparison will utilize GEANT4 simulations alongside standard point-type gamma-ray sources.

Key words: 4π multi-detectors array, geometrical solid angle, total efficiency, average path length

INTRODUCTION

The NaI(Tl) scintillation crystals are available in single and polycrystalline forms, exhibiting a high light production. Furthermore, they demonstrate negligible self-absorption of scintillation light. The emission spectrum aligns effectively with the sensitivity characteristics of bialkali photocathodes used in photomultiplier tubes (PMT) [1-3]. The NaI(Tl) detectors exhibit exceptionally high luminescence efficiency and can be fabricated in different dimensions and geometries. This versatility makes them the most commonly used scintillators in various applications. Thallium-doped NaI scintillator produces one of the highest signals in a photomultiplier tube for a given amount of absorbed radiation. Under optimal conditions, approximately 10^4 photoelectrons are generated per 1 MeV gamma-ray energy [4-6]. The NaI(Tl) exhibits multiple decay time constant mechanisms. The primary single exponential decay constant at room temperature is approximately 250 ns. As temperature rises, the longer time constant components and the response curves converge, reducing the decay time from 1 ms to 12 ms [7, 8].

The scintillation crystal should not be subjected to ultraviolet (UV) radiation from sunlight or luminous lamps, as such exposure can significantly impair and diminish the scintillation performance [9, 10]. The NaI(Tl) scintillation crystals are routinely manufactured with potassium concentrations below 0.5 parts per million (ppm), which makes them particularly suitable for low background applications. These NaI(Tl) crystals are extensively used in various radiation detection applications.

* Corresponding author, e-mail: ms241178@hotmail.com

They are particularly prevalent in well logging, environmental monitoring, nuclear medicine, aerial surveys, and nuclear physics, among several other applications [11-13]. In summary, protecting scintillation crystals from UV exposure and moisture is essential. Furthermore, the development of low-potassium sodium iodide doped with thallium NaI(Tl) crystals enhances their effectiveness in sensitive detection applications. Currently, polycrystalline NaI(Tl) scintillation detectors are increasingly recognized as viable alternatives to single-crystal scintillators in various applications where mechanical and thermal shocks are prevalent, such as in gas exploration and oil extraction. These detectors offer a combination of robustness and scintillation performance comparable to that of single-crystal NaI(Tl) detectors [5, 14].

The polycrystalline configuration of NaI(Tl) is produced through a well-defined process in which single-crystal bricks are recrystallized under applied pressure and heat. The resulting material can be characterized as a polycrystalline substance comprising randomly oriented crystal particles within a mixed structural framework [5, 15]. The density of NaI remains unchanged during the development process. This characteristic enhances the mechanical strength of the material without impacting the performance of the scintillation process, as the optical properties of NaI(Tl) in polycrystalline form are comparable to those of single-crystal NaI(Tl) [5, 16]. Cracks that occur due to mechanical or thermal shock in NaI(Tl) polycrystals are typically confined to small local regions known as grains. Since the cleavage planes of the grains are randomly oriented, it is unlikely that a small crack would propagate across the grain boundaries. This characteristic makes NaI(Tl) polycrystalline material a preferred choice in applications where durability is critical, such as aerospace and well-logging [5, 17-19].

In contrast, single crystals can fracture along specific planes under stress. In a detector assembly composed of single crystal material, even a minor crack can propagate throughout the entire crystal, adversely affecting signal height resolution and the light collection process [5, 20, 21]. In nuclear physics, the prompt gamma neutron activation analysis (PGNAA) technique is recognized as a highly effective method for simultaneously determining the quantity and presence of multiple elements in samples with masses ranging from micrograms to several grams. This non-destructive technique is minimally affected by the sample's physical shape and chemical composition. Classic measurements were obtained over durations ranging from several minutes to a few hours for each sample under investigation [22-24]. The technique can be described as the sample is irradiated with a narrow beam of neutrons. The constituent elements within the sample capture a portion of these neutrons, resulting in the emission of prompt gamma rays, which are precisely measured using a gamma-ray NaI(Tl) or HPGe spectrometer.

The energies of the emitted gamma-rays identify the neutron-capturing elements, while the intensities of the gamma-ray peaks at these energies indicate their concentrations. The quantity of the elements under investigation is determined by the ratio of the count rate of the peak of interest in the sample to the count rate of a known mass of an appropriate elemental standard irradiated under identical conditions [25-27]. Typically, the sample will not acquire significant long-lived radioactivity, allowing for its potential removal from the irradiated facility for additional applications. One of the primary uses of PGNAA is as a mass material analyzer in the coal, mineral, and cement industries [28-30]. At the Institute for Nuclear Research and Nuclear Energy of the Bulgarian Academy of Sciences, a NaI(Tl) scintillator crystal system, designed in the shape of a daisy flower (referred to as *Romashka*), has been constructed and tested [31, 32]. This system can investigate radiative neutron capture and fission reactions [33, 34] involving various mono-isotopes that are important to nuclear science and its applications. The incorporation of high-quality lead shielding renders the system suitable for operation as a low-background radiation detector, facilitating the measurement of natural radioactivity in environmental material samples [35]. Additionally, it can be utilized for elemental analysis of samples in conjunction with the resonance neutron time-of-flight spectrometer IREN at the Frank Laboratory of Neutron Physics of the Joint Institute for Nuclear Research [36]. In both types of investigations, the potential application of the gamma- -multiplicity method warrants exploration [37].

In all the aforementioned applications, accurate values of gamma-ray detection efficiency for NaI(Tl) or HPGe spectrometers at specific gamma energies are essential. Mitigating interference from different gamma energies requires a thorough understanding of the detector's resolution corresponding to these energies [18, 19]. Resolution and detection efficiency values vary depending on the detector size and other parameters. Therefore, it is imperative to ascertain these values for a specific detector before its application in quantitative investigations [20, 21]. This study focuses on the calculation of the solid angle, effective solid angle, and efficiency of a *Romashka* module using an analytical numerical technique. Additionally, it investigates the average path length within the detector materials as a function of the source position. The 12 NaI(Tl) scintillator gamma detectors form a specialized 4π multi-detector array system (NaGRaDA) that differs from conventional and well-known multi-detector gamma-ray spectrometers in both shape and size. This 4π system enables the measurement of samples with extremely low gamma activity and is applicable in conventional instrumental neutron activation analysis (INAA) and prompt-gamma neutron activation analysis. The results may provide valuable insights for applications in radiation detection and nuclear physics. Additionally, they can inform scientists regarding the optimization and design of detection setups tailored to specific experimental conditions.

MATHEMATICAL VIEWPOINT

The analytical numerical technique has been employed to estimate the solid angle, effective solid angle, efficiency of the *Romashka* NaI(Tl) module, and the average gamma-ray path length within the materials of the detector, contingent upon the position of the source. The general expression for the geometric solid angle, denoted as Ω_G, formed between a radioactive source and a *Romashka* NaI(Tl) gamma-ray detector module, in a spherical coordinate system, is represented by the following eq.

$$\Omega_G = \int_{\varphi}\int_{\theta} \sin\theta \, \mathrm{d}\theta \, \mathrm{d}\varphi \tag{1}$$

The geometrical efficiency of a *Romashka* gamma-ray detector module, ε_G, is defined as

$$\varepsilon_G = \frac{\Omega_G}{4\pi} \tag{2}$$

The total efficiency, denoted as of a *Romashka* NaI(Tl) gamma-ray detector module in relation to radioactive sources, is represented by the following eq.

$$\varepsilon_{T(axial)} = \frac{\Omega_{eff}}{4\pi} \tag{3}$$

where Ω_{eff} a denotes the effective solid angle between the source and the detector, accounting for all materials between the source and the detector, as well as the detector material itself. To calculate the efficiency of the *Romashka* NaI(Tl) gamma-ray detector model, one must consider the positioning of the radioactive source concerning the detector. Furthermore, this analysis will address all potential scenarios involving the utilization of a radioactive point source, which will be discussed in next sections.

Case I: ($h \geq L$)

The radioactive point source is positioned above the detector surface at a height ($h \geq L$), where L represents the side length of the detector, as illustrated in fig. 1.

The effective solid angle, denoted as Ω_{eff}, will take one of the following expressions, ranging from (a) to (e), depending on the values of the polar angle.

$$\text{(a)}\ \theta_5 > \theta_4 > \theta_3 > \theta_6 > \theta_2$$

$$\Omega_{eff} = \int_0^{\frac{\pi}{3}} \left[\int_{\theta_1}^{\theta_2} f_1 \sin\theta \mathrm{d}\theta + \int_{\theta_2}^{\theta_6} f_2 \sin\theta \mathrm{d}\theta + \int_{\theta_6}^{\theta_3} f_4 \sin\theta \mathrm{d}\theta + \right.$$
$$\left. + \int_{\theta_3}^{\theta_4} f_5 \sin\theta \mathrm{d}\theta + \int_{\theta_4}^{\theta_5} f_8 \sin\theta \mathrm{d}\theta + \int_{\theta_5}^{\theta_7} f_{10} \sin\theta \mathrm{d}\theta \right] \mathrm{d}\varphi \tag{4}$$

$$\text{(b)}\ \theta_5 > \theta_4 > \theta_6 > \theta_3 > \theta_2$$

$$\Omega_{eff} = \int_0^{\frac{\pi}{3}} \left[\int_{\theta_1}^{\theta_2} f_1 \sin\theta \mathrm{d}\theta + \int_{\theta_2}^{\theta_3} f_2 \sin\theta \mathrm{d}\theta + \int_{\theta_3}^{\theta_6} f_3 \sin\theta \mathrm{d}\theta + \right.$$
$$\left. + \int_{\theta_6}^{\theta_4} f_5 \sin\theta \mathrm{d}\theta + \int_{\theta_4}^{\theta_5} f_8 \sin\theta \mathrm{d}\theta + \int_{\theta_5}^{\theta_7} f_{10} \sin\theta \mathrm{d}\theta \right] \mathrm{d}\varphi \tag{5}$$

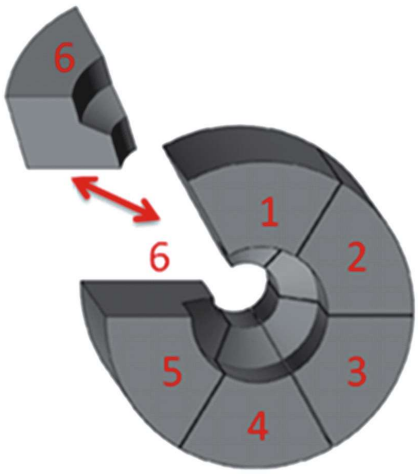

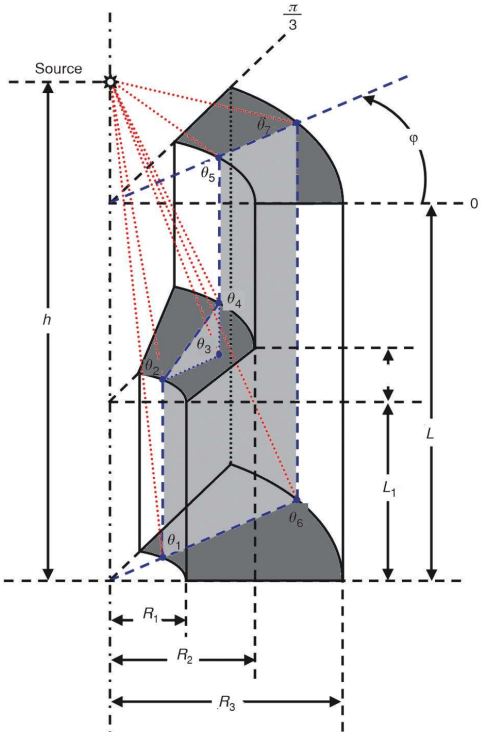

Figure 1. Radioactive point source at axial position ($h \geq L$)

(c) $\theta_5 > \theta_6 > \theta_4 > \theta_3 > \theta_2$

$$\Omega_{\text{eff}} = \int_0^{\frac{\pi}{3}} \left[\int_{\theta_1}^{\theta_2} f_1 \sin\theta \,\mathrm{d}\theta + \int_{\theta_2}^{\theta_3} f_2 \sin\theta \,\mathrm{d}\theta + \int_{\theta_3}^{\theta_4} f_3 \sin\theta \,\mathrm{d}\theta + \int_{\theta_4}^{\theta_6} f_6 \sin\theta \,\mathrm{d}\theta + \int_{\theta_6}^{\theta_5} f_8 \sin\theta \,\mathrm{d}\theta + \int_{\theta_5}^{\theta_7} f_{10} \sin\theta \,\mathrm{d}\theta \right] \mathrm{d}\varphi \quad (6)$$

(d) $\theta_6 > \theta_5 > \theta_4 > \theta_3 > \theta_2$

$$\Omega_{\text{eff}} = \int_0^{\frac{\pi}{3}} \left[\int_{\theta_1}^{\theta_2} f_1 \sin\theta \,\mathrm{d}\theta + \int_{\theta_2}^{\theta_3} f_2 \sin\theta \,\mathrm{d}\theta + \int_{\theta_3}^{\theta_4} f_3 \sin\theta \,\mathrm{d}\theta + \int_{\theta_4}^{\theta_5} f_6 \sin\theta \,\mathrm{d}\theta + \int_{\theta_5}^{\theta_6} f_7 \sin\theta \,\mathrm{d}\theta + \int_{\theta_6}^{\theta_7} f_{10} \sin\theta \,\mathrm{d}\theta \right] \mathrm{d}\varphi \quad (7)$$

(e) $\theta_5 > \theta_4 > \theta_3 > \theta_2 > \theta_6$

$$\Omega_{\text{eff}} = \int_0^{\frac{\pi}{3}} \left[\int_{\theta_1}^{\theta_6} f_1 \sin\theta \,\mathrm{d}\theta + \int_{\theta_6}^{\theta_2} f_9 \sin\theta \,\mathrm{d}\theta + \int_{\theta_2}^{\theta_3} f_4 \sin\theta \,\mathrm{d}\theta + \int_{\theta_3}^{\theta_4} f_5 \sin\theta \,\mathrm{d}\theta + \int_{\theta_4}^{\theta_5} f_8 \sin\theta \,\mathrm{d}\theta + \int_{\theta_5}^{\theta_7} f_{10} \sin\theta \,\mathrm{d}\theta \right] \mathrm{d}\varphi \quad (8)$$

The parameter f_i can be represented as follows

$$f_i = (1 - e^{-\mu d_i}) f_{\text{att}} \quad (9)$$

The f_i values depend on the path length of the photon, as shown in fig. 2, through the detector material d_i. This relationship takes on ten distinct expressions, which are as follows

$$\begin{aligned}
d_1 &= \frac{L_1}{\cos(\theta)} - \frac{R_1}{\sin(\theta)} + \frac{h - L_1}{\cos(\theta)} \\
d_2 &= BC + \frac{L_1}{\cos(\theta)} \\
d_3 &= BC' + \left[\frac{L}{\cos(\theta)} - \frac{R_2}{\sin(\theta)} + \frac{h - L}{\cos(\theta)} \right] \\
d_4 &= BC + \left[\frac{R_3}{\sin(\theta)} - \frac{h - L_1}{\cos(\theta)} \right] \\
d_5 &= BC' + \left[\frac{R_3}{\sin(\theta)} - \frac{R_2}{\sin(\theta)} \right] \\
d_6 &= \frac{L}{\cos(\theta)} - \frac{R_2}{\sin(\theta)} + \frac{h - L}{\cos(\theta)} \\
d_7 &= \frac{L}{\cos(\theta)} \\
d_8 &= \frac{R_3}{\sin(\theta)} - \frac{R_2}{\sin(\theta)} \\
d_9 &= \frac{R_3}{\sin(\theta)} - \frac{R_1}{\sin(\theta)} \\
d_{10} &= \frac{R_3}{\sin(\theta)} - \frac{h - L}{\cos(\theta)}
\end{aligned} \quad (10)$$

The factor μ represents the total attenuation coefficient of the detector material. Additionally, f_{att} denotes the attenuation effect of all absorbers located between the source and the detector material. The relationship can be expressed as follows

$$\begin{aligned}
&\text{for horizontal absorbers} && f_{\text{att}} = \mathrm{e}^{-\sum_{i=1}^{x} \left(\frac{\mu_i t_i}{\cos(\theta)} \right)} \\
&\text{for vertical absorbers} && f_{\text{att}} = \mathrm{e}^{-\sum_{i=1}^{x} \left(\frac{\mu_i t_i}{\sin(\theta)} \right)} \\
&\text{for inclinde absorbers by angle (x)} && f_{\text{att}} = \mathrm{e}^{-\sum_{i=1}^{x} \left(\frac{\mu_i t_i}{\cos(\theta - x)} \right)}
\end{aligned} \quad (11)$$

The terms μ_i and t_i represent the total attenuation coefficient and the thickness of the i^{th} absorber, respectively. The BC and BC' parameters are shown in fig. 3, and they can be obtained using the following expressions

$$\begin{aligned}
BC &= \frac{h - L_1}{\cos(\theta)} - \left(\frac{h - L_1 - L_2}{\cos\theta_4} \right) \left(\frac{\cos(x - \theta_4)}{\cos(x - \theta)} \right) \\
BC' &= \frac{R_2}{\cos\left(\frac{\pi}{2} - \theta \right)} - \left(\frac{h - L_1 - L_2}{\cos\theta_4} \right) \left(\frac{\cos(x - \theta_4)}{\cos(x - \theta)} \right)
\end{aligned} \quad (12)$$

All path lengths are influenced by the polar angles θ which are represented by seven distinct expressions delineated in the subsequent equations

$$\begin{aligned}
\theta_1 &= \tan^{-1}\left(\frac{R_1}{h} \right) \\
\theta_2 &= \tan^{-1}\left(\frac{R_1}{h - L_1} \right) \\
\theta_3 &= \tan^{-1}\left(\frac{R_2}{h - L_1} \right) \\
\theta_4 &= \tan^{-1}\left(\frac{R_2}{h - L_1 - L_2} \right) \\
\theta_5 &= \tan^{-1}\left(\frac{R_2}{h - L} \right) \\
\theta_6 &= \tan^{-1}\left(\frac{R_3}{h} \right) \\
\theta_7 &= \tan^{-1}\left(\frac{R_3}{h} \right)
\end{aligned} \quad (13)$$

Case II: ($L > h \geq L_1 + L_2$)

The radioactive point source is placed below the detector surface at position ($L > h \geq L_1 + L_2$), where, L_1, and, L_2, are illustrated as shown in fig. 4.

The effective solid angle Ω_{eff} will take one of the following expressions, from (a) to (d), based on the polar angle values

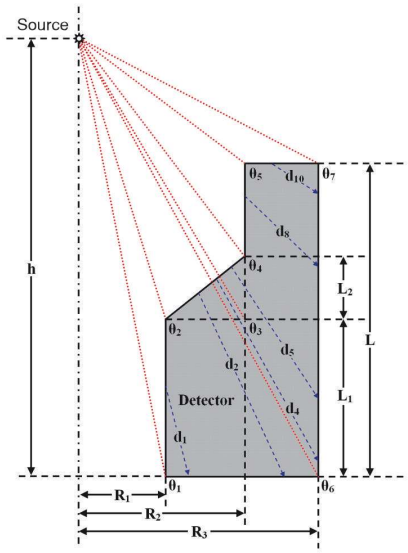

(a) $\theta_5 > \theta_4 > \theta_3 > \theta_6 > \theta_2$

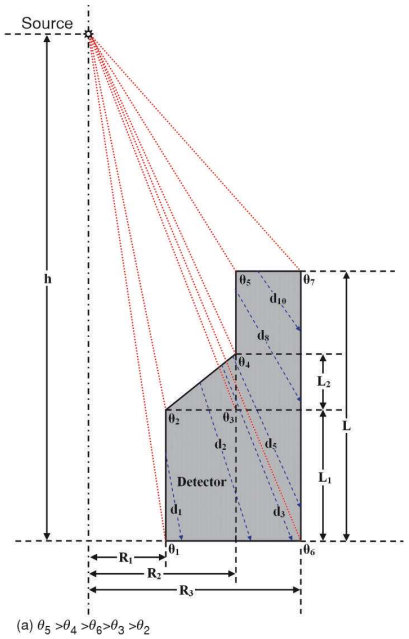

(a) $\theta_5 > \theta_4 > \theta_6 > \theta_3 > \theta_2$

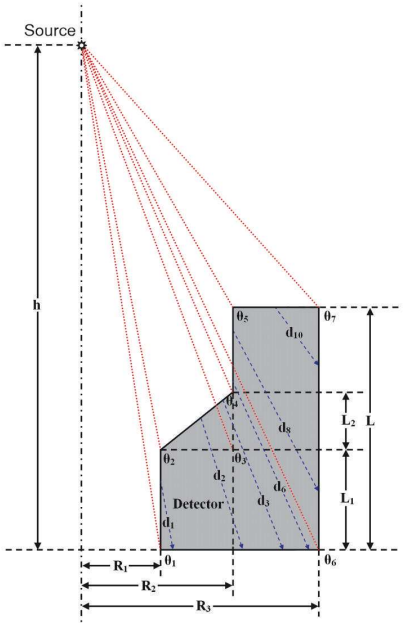

c) $\theta_5 > \theta_6 > \theta_4 > \theta_3 > \theta_2$

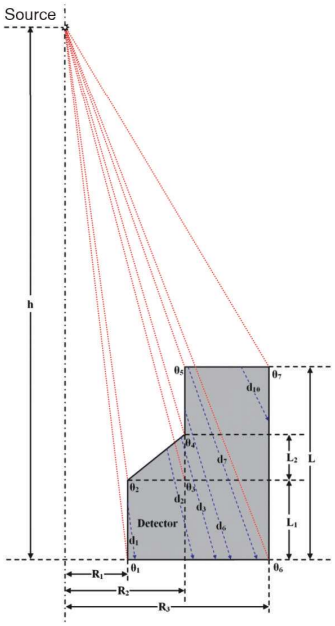

(d) $\theta_6 > \theta_5 > \theta_4 > \theta_3 > \theta_2$

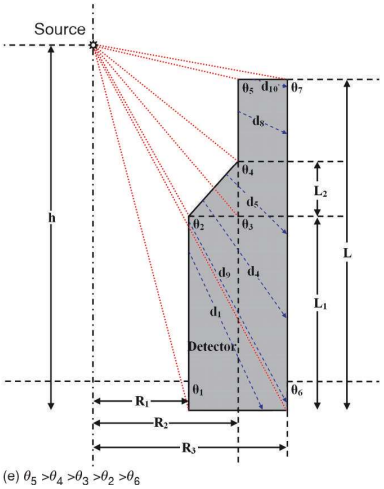

(e) $\theta_5 > \theta_4 > \theta_3 > \theta_2 > \theta_6$

Figure 2. The five possible cases of radioactive point source placed at axial position ($h \geq L$)

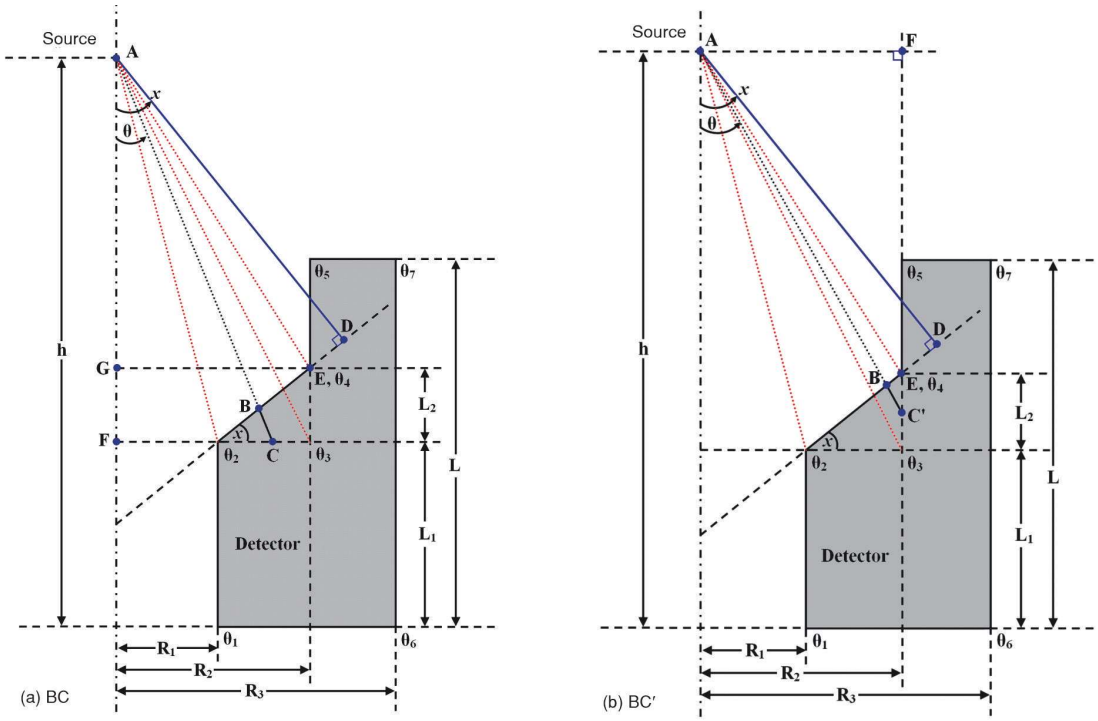

Figure 3. Schematic view of the parameters BC and BC

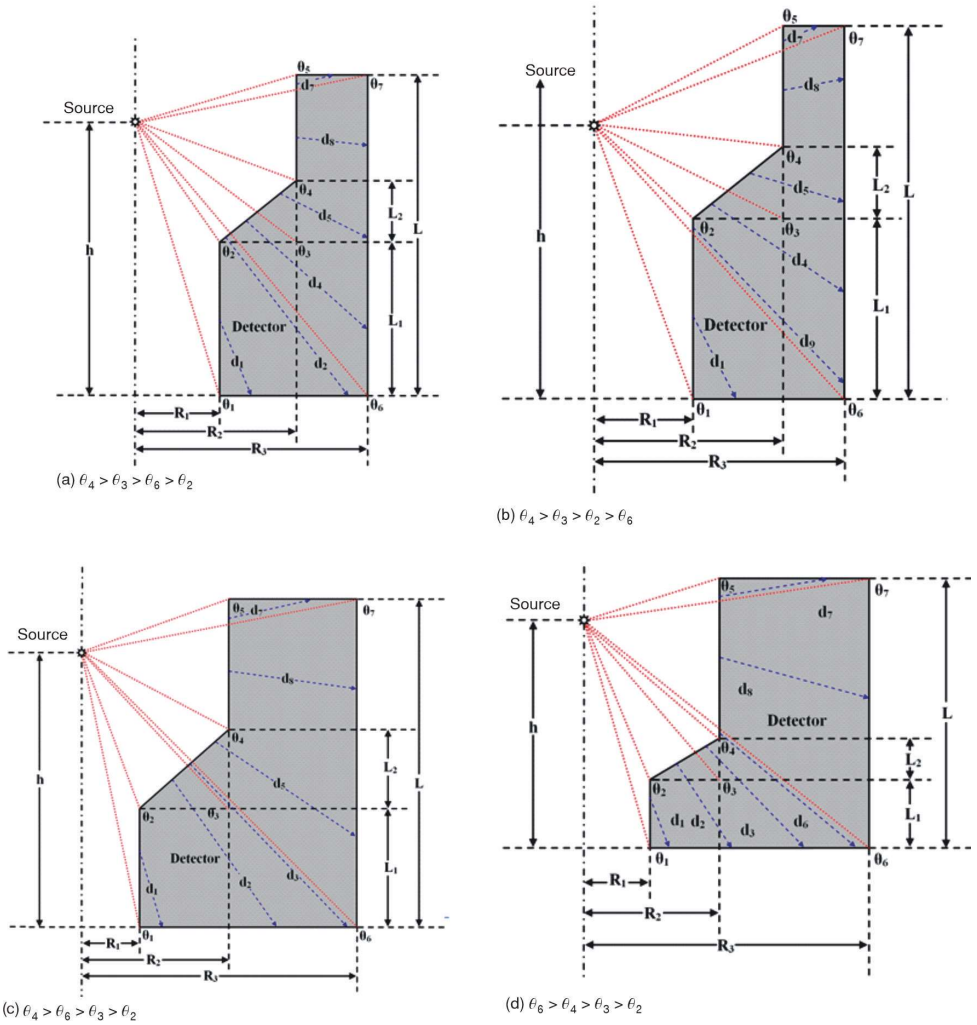

Figure 4. The four possible cases of a radioactive point source placed at an axial position ($L > h \geq L_1 + L_2$)

(a) $\theta_4 > \theta_3 > \theta_6 > \theta_2$

$$\Omega_{\text{eff}} = \int_0^{\frac{\pi}{3}} \left[\int_{\theta_1}^{\theta_2} f_1 \sin\theta \mathrm{d}\theta + \int_{\theta_2}^{\theta_6} f_2 \sin\theta \mathrm{d}\theta + \int_{\theta_6}^{\theta_3} f_4 \sin\theta \mathrm{d}\theta + \int_{\theta_3}^{\theta_4} f_5 \sin\theta \mathrm{d}\theta + \int_{\theta_4}^{\theta_7} f_8 \sin\theta \mathrm{d}\theta + \int_{\theta_7}^{\theta_5} f_7 \sin\theta \mathrm{d}\theta \right] \mathrm{d}\varphi \quad (14)$$

(b) $\theta_4 > \theta_3 > \theta_2 > \theta_6$

$$\Omega_{\text{eff}} = \int_0^{\frac{\pi}{3}} \left[\int_{\theta_1}^{\theta_6} f_1 \sin\theta \mathrm{d}\theta + \int_{\theta_6}^{\theta_2} f_9 \sin\theta \mathrm{d}\theta + \int_{\theta_2}^{\theta_3} f_4 \sin\theta \mathrm{d}\theta + \int_{\theta_3}^{\theta_4} f_5 \sin\theta \mathrm{d}\theta + \int_{\theta_4}^{\theta_7} f_8 \sin\theta \mathrm{d}\theta + \int_{\theta_7}^{\theta_5} f_7 \sin\theta \mathrm{d}\theta \right] \mathrm{d}\varphi \quad (15)$$

(c) $\theta_4 > \theta_6 > \theta_3 > \theta_2$

$$\Omega_{\text{eff}} = \int_0^{\frac{\pi}{3}} \left[\int_{\theta_1}^{\theta_2} f_1 \sin\theta \mathrm{d}\theta + \int_{\theta_2}^{\theta_3} f_2 \sin\theta \mathrm{d}\theta + \int_{\theta_3}^{\theta_6} f_3 \sin\theta \mathrm{d}\theta + \int_{\theta_6}^{\theta_4} f_5 \sin\theta \mathrm{d}\theta + \int_{\theta_4}^{\theta_7} f_8 \sin\theta \mathrm{d}\theta + \int_{\theta_7}^{\theta_5} f_7 \sin\theta \mathrm{d}\theta \right] \mathrm{d}\varphi \quad (16)$$

(d) $\theta_6 > \theta_4 > \theta_3 > \theta_2$

$$\Omega_{\text{eff}} = \int_0^{\frac{\pi}{3}} \left[\int_{\theta_1}^{\theta_2} f_1 \sin\theta \mathrm{d}\theta + \int_{\theta_2}^{\theta_3} f_2 \sin\theta \mathrm{d}\theta + \int_{\theta_3}^{\theta_4} f_3 \sin\theta \mathrm{d}\theta + \int_{\theta_4}^{\theta_6} f_6 \sin\theta \mathrm{d}\theta + \int_{\theta_6}^{\theta_7} f_8 \sin\theta \mathrm{d}\theta + \int_{\theta_7}^{\theta_5} f_7 \sin\theta \mathrm{d}\theta \right] \mathrm{d}\varphi \quad (17)$$

The parameter f_i can be obtained as previously defined in eq. (9). The f_i values depend on the path length of a photon through the detector material, d_i, which will take nine different expressions as follows

$$\begin{aligned}
d_1 &= \frac{L_1}{\cos(\theta)} - \frac{R_1}{\sin(\theta)} + \frac{h - L_1}{\cos(\theta)} \\
d_2 &= BC + \frac{L_1}{\cos(\theta)} \\
d_3 &= BC' + \left[\frac{L_1 + L_2}{\cos(\theta)} + \frac{R_2}{\sin(\theta)} + \frac{h - L_1 - L_2}{\cos(\theta)} \right] \\
d_4 &= BC + \left[\frac{R_3}{\sin(\theta)} - \frac{h - L_1}{\cos(\theta)} \right] \\
d_5 &= BC' + \left[\frac{R_3}{\sin(\theta)} - \frac{R_2}{\sin(\theta)} \right] \\
d_6 &= \frac{h}{\cos(\theta)} - \frac{R_2}{\sin(\theta)} \\
d_7 &= \frac{L - h}{\cos(\pi - \theta)} - \frac{R_2}{\sin(\pi - \theta)} \\
d_8 &= \frac{R_3}{\sin(\theta)} - \frac{R_2}{\sin(\theta)} \\
d_9 &= \frac{R_3}{\sin(\theta)} - \frac{R_1}{\sin(\theta)}
\end{aligned} \quad (18)$$

The polar angles θ in these cases will be redefined to align with the new source-to-detector position. Seven expressions are presented in the following equations

$$\begin{aligned}
\theta_1 &= \tan^{-1}\left(\frac{R_1}{h}\right) \\
\theta_2 &= \tan^{-1}\left(\frac{R_1}{h - L_1}\right) \\
\theta_3 &= \tan^{-1}\left(\frac{R_2}{h - L_1}\right) \\
\theta_4 &= \tan^{-1}\left(\frac{R_2}{L_1 + L_2 - h}\right) \\
\theta_5 &= \pi - \tan^{-1}\left(\frac{R_2}{L - h}\right) \\
\theta_6 &= \tan^{-1}\left(\frac{R_3}{h}\right) \\
\theta_7 &= \pi - \tan^{-1}\left(\frac{R_3}{L - h}\right)
\end{aligned} \quad (19)$$

Case III: ($L_1 + L_2 > h \geq L_1$)

The radioactive point source is placed below the detector surface at the position ($L_1 + L_2 > h \geq L_1$), as shown in fig. 5. The effective solid angle Ω_{eff} is given by one of the following expressions, from (a) to (c), depending on the polar angle values

(a) $\theta_4 > \theta_3 > \theta_2 > \theta_6$

$$\Omega_{\text{eff}} = \int_0^{\frac{\pi}{3}} \left[\int_{\theta_1}^{\theta_6} f_1 \sin\theta \mathrm{d}\theta + \int_{\theta_6}^{\theta_2} f_2 \sin\theta \mathrm{d}\theta + \int_{\theta_2}^{\theta_1} f_3 \sin\theta \mathrm{d}\theta + \int_{\theta_3}^{\theta_4} f_5 \sin\theta \mathrm{d}\theta + \int_{\theta_4}^{\theta_7} f_8 \sin\theta \mathrm{d}\theta + \int_{\theta_7}^{\theta_5} f_7 \sin\theta \mathrm{d}\theta \right] \mathrm{d}\varphi \quad (20)$$

(b) $\theta_4 > \theta_6 > \theta_3 > \theta_2$

$$\Omega_{\text{eff}} = \int_0^{\frac{\pi}{3}} \left[\int_{\theta_1}^{\theta_2} f_1 \sin\theta \mathrm{d}\theta + \int_{\theta_2}^{\theta_3} f_2 \sin\theta \mathrm{d}\theta + \int_{\theta_3}^{\theta_6} f_3 \sin\theta \mathrm{d}\theta + \int_{\theta_6}^{\theta_4} f_5 \sin\theta \mathrm{d}\theta + \int_{\theta_4}^{\theta_7} f_8 \sin\theta \mathrm{d}\theta + \int_{\theta_7}^{\theta_5} f_7 \sin\theta \mathrm{d}\theta \right] \mathrm{d}\varphi \quad (21)$$

(c) $\theta_4 > \theta_3 > \theta_6 > \theta_2$

$$\Omega_{\text{eff}} = \int_0^{\frac{\pi}{3}} \left[\int_{\theta_1}^{\theta_2} f_1 \sin\theta \mathrm{d}\theta + \int_{\theta_2}^{\theta_6} f_2 \sin\theta \mathrm{d}\theta + \int_{\theta_6}^{\theta_3} f_4 \sin\theta \mathrm{d}\theta + \int_{\theta_3}^{\theta_4} f_5 \sin\theta \mathrm{d}\theta + \int_{\theta_4}^{\theta_7} f_8 \sin\theta \mathrm{d}\theta + \int_{\theta_7}^{\theta_5} f_7 \sin\theta \mathrm{d}\theta \right] \mathrm{d}\varphi \quad (22)$$

The parameter f_i can be obtained as previously defined in eq. (9). Also, the path length of a photon through the detector material d_i will take nine different expressions as follows

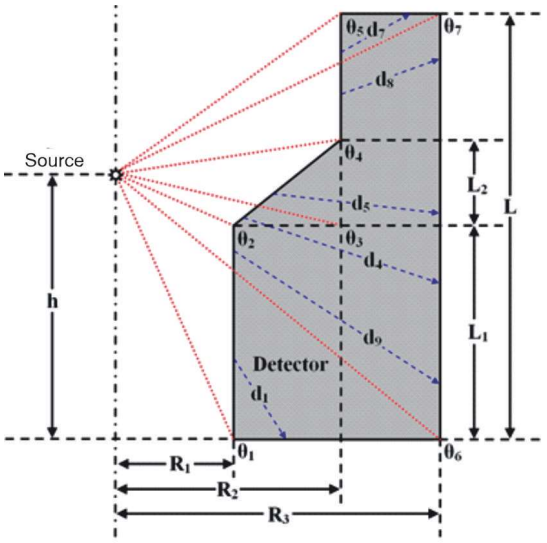

(a) $\theta_4 > \theta_3 > \theta_2 > \theta_6$

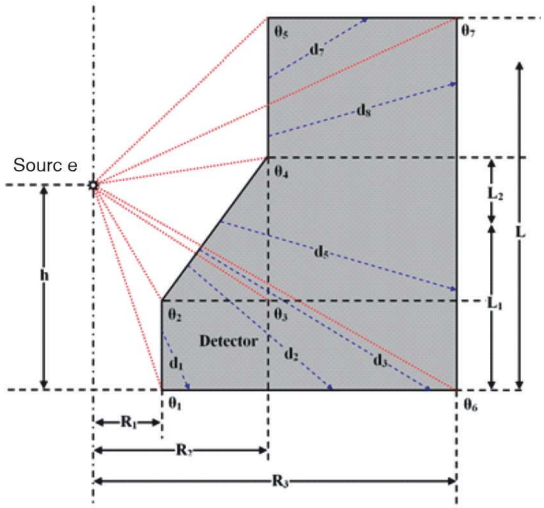

(b) $\theta_4 > \theta_6 > \theta_3 > \theta_2$

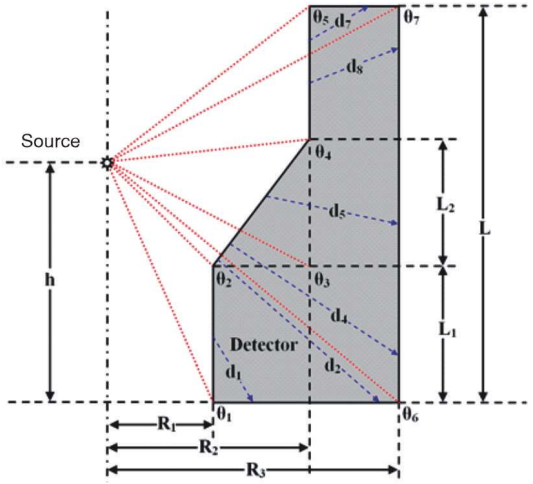

(c) $\theta_4 > \theta_3 > \theta_6 > \theta_2$

Figure 5. The three possible cases of a radioactive point source placed at an axial ($L_1 + L_2 > h \geq L_1$)

$$
\begin{aligned}
d_1 &= \frac{L_1}{\cos\theta} - \frac{R_1}{\sin\theta} + \frac{h-L_1}{\cos\theta} \\
d_2 &= BC + \frac{L_1}{\cos\theta} \\
d_3 &= BC' + \left[\frac{L_1+L_2}{\cos\theta} + \frac{R_2}{\sin\theta} + \frac{h-L_1-L_2}{\cos\theta}\right] \\
d_4 &= BC + \left[\frac{R_3}{\sin\theta} - \frac{h-L_1}{\cos\theta}\right] \\
d_5 &= BC' + \left[\frac{R_3}{\sin\theta} - \frac{R_2}{\sin\theta}\right] \\
d_6 &= \frac{h}{\cos\theta} - \frac{R_2}{\sin\theta} \\
d_7 &= \frac{L-h}{\cos(\pi-\theta)} - \frac{R_2}{\sin(\pi-\theta)} \\
d_8 &= \frac{R_3}{\sin\theta} - \frac{R_2}{\sin\theta} \\
d_9 &= \frac{R_3}{\sin\theta} - \frac{R_1}{\sin\theta}
\end{aligned}
\tag{23}
$$

The new polar angles θ in these cases will be defined as presented in the following eq.

$$
\begin{aligned}
\theta_1 &= \tan^{-1}\left(\frac{R_1}{h}\right) \\
\theta_2 &= \tan^{-1}\left(\frac{R_1}{h-L_1}\right) \\
\theta_3 &= \tan^{-1}\left(\frac{R_2}{h-L_1}\right) \\
\theta_4 &= \pi - \tan^{-1}\left(\frac{R_2}{L_1+L_2-h}\right) \\
\theta_5 &= \pi - \tan^{-1}\left(\frac{R_2}{L-h}\right) \\
\theta_6 &= \tan^{-1}\left(\frac{R_3}{h}\right) \\
\theta_7 &= \pi - \tan^{-1}\left(\frac{R_3}{L-h}\right)
\end{aligned}
\tag{24}
$$

The average path length $\bar{d}_{(axial)}$ in the detector for using an axial radioactive point source can be calculated according to the following eq.

$$\bar{d}_{(axial)} = \frac{\int_{\Omega_G} [d_i(\theta) \mathrm{d}\Omega_G}{\int_{\Omega_G} \mathrm{d}\Omega_G} = \frac{\int_0^{\frac{\pi}{3}} \int_0^{\theta_{max}} [d_i(\theta)] \sin\theta \mathrm{d}\theta \mathrm{d}\varphi}{\int_0^{\frac{\pi}{3}} \int_0^{\theta_{max}} \sin\theta \mathrm{d}\theta \mathrm{d}\varphi} \quad (25)$$

The parameter θ_{max} is equal to θ_7 in case (I), while it is equal to θ_5 in cases (II and III).

THE NaGRaDA MODULES DESCRIPTION

A 4π NaGRaDA featuring a *Romashka*-like arrangement of multiple scintillators was specifically designed to facilitate sensitive gamma-ray measurements of low-activity environmental samples and neutron-induced nuclear reactions. This configuration offers a high-efficiency detection solution tailored for research applications [31, 32]. The system comprises 12 NaI(Tl) scintillators, arranged in two halves. Each half contains six uniquely shaped crystals that resemble the petals of a *Romashka*, as illustrated in fig. 6. The total volume of the NaI(Tl) crystals is 16.6 L, contained within a cylindrical casing with an outer diameter of 30 cm. The *Romashka* crystal configuration serves effectively as a full absorption detector for gamma quanta. The scintillations produced by each crystal are transmitted through a light guide to a photomultiplier tube for detection. The pulses are transmitted to a charge preamplifier, where the amplified signals undergo further processing. These signals can be either summed to produce an amplitude or directed to a multichannel analyzer. At this stage, they can be analyzed directly or processed by an accompanying analysis computer.

The signal processing and data collection capabilities of the upgraded version of the previous *Romashka* system will feature a computerized 32 channel digital readout system. This system will utilize two ADCM16-LTC (16-channel, 14-bit, 100 MHz) ADC boards from AFI Electronics© [38], similar to those employed in the TANGRA-NaI(Tl) setup [39]. The digitized signals will be transmitted through the PCI-E bus into the computer's memory, where data processing and storage will occur. The system's maximum capacity is approximately 105 events per second [39, 40]. Some drawings of a *Romashka* scintillation unit are shown in fig. 7. The NaGRaDA main modules are shown as the collage picture in fig. 8, where: 1 – six NaI(Tl) crystals in a single Al cylinder wrapped with Al arc-seals, 2 – photo multiplier tubes FEU-110 and high-voltage divider, 3 – Pb shielding-collimator, 4 and 5 – lower and upper Pb shielding arcs, 6 – adjustable rigid iron support, 7 – movable iron trolley, 8 – 16 channels HVSys power supply, 9 – Parsek Desktop 4k MCA [41], 10 – fast PC with two ADCM-16 boards, 11 – 16-channel, 14-bit, 100 MHz ADC-board [42], and 12 – laptop with operational software of PMTs' power supply.

RESULTS AND DISCUSSION

The analytical numerical technique is a straightforward method for calculating solid angles, effective solid angles, and the efficiency of the *Romashka*

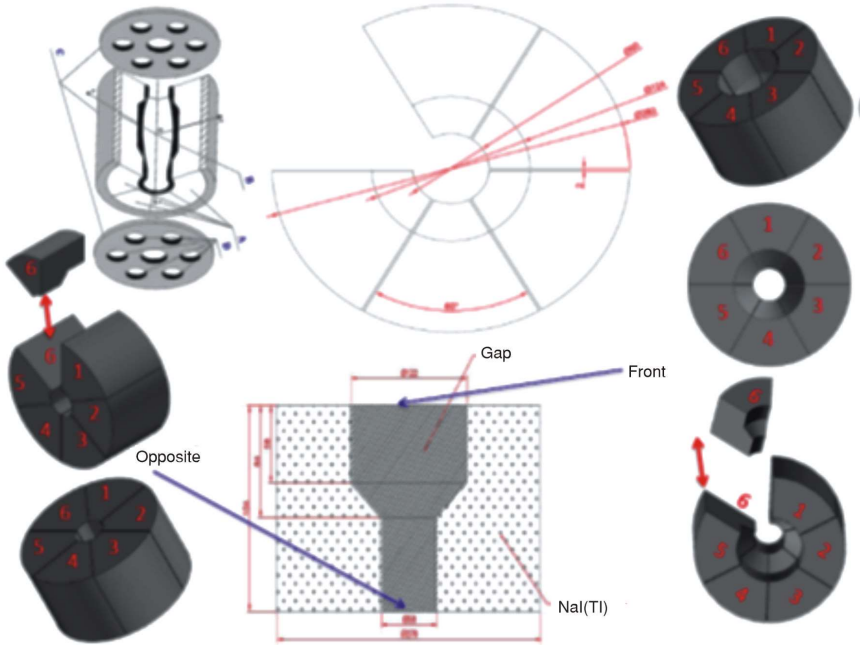

Figure 6. Schematic drawing of a NaGRaDA *Romashka* module

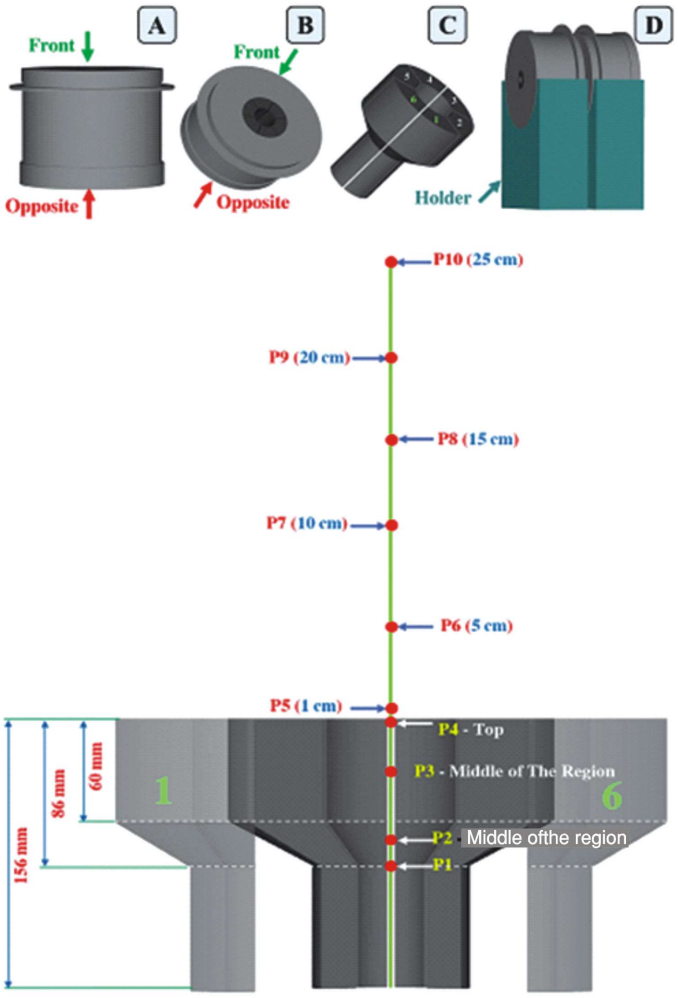

Figure 7. The drawings of a *Romashka* scintillation unit include: A – a through cavity for placing filters, absorbers, and samples, B – the module casing, C – NaI(Tl) crystals, D – both modules positioned side-by-side. P1 to P10 indicate possible positions for the radioactive point source, inside and outside the unit cavity

NaI(Tl) multi-crystal units. Additionally, it facilitates the determination of the average path length within the detector's materials, contingent upon the positioning of the radioactive point source. The trapezoidal rule was employed as the numerical method to compute systematic integrations with high accuracy. This method partitions the integration into a large set of intervals ($n = 100$) and is implemented using a programming language. The analytical numerical method enables technicians and scientists to assist in the construction and testing of gamma-ray detectors. Furthermore, it facilitates the evaluation of control processes governing the reproduction of specialized scintillator designs and their responses to radiation measurements.

In this study, the radioactive point source is intended to cover distances ranging from P1 to P10, as illustrated in fig. 7. Some of these distances are positioned both within and outside the crystal cavity of the *Romashka* NaI(Tl) unit. This comprehensive approach aims to encompass all potential scenarios for real measurements. The effective solid angle, Ω_{eff}, between the radioactive point source and the cavity of the *Romashka* NaI(Tl) unit for various locations is depicted in fig.7 and detailed in fig. 9. This estimation is based on cases (I), (II), and (III) and is presented as a function of photon energy, ranging from 0.05 MeV to 10 MeV. The effective solid angle, Ω_{eff}, reaches its maximum value at source position P1, located within the detector cavity. As the source moves away from P1 and approaches P10, which is situated outside the detector cavity, the effective solid angle Ω_{eff} gradually decreases, ultimately reaching its minimum at this external position. In addition, the effective solid angle Ω_{eff} increases beyond 6 MeV, while NaI(Tl) continues to rise in the high-energy region, reaching up to 10 MeV.

It can be observed that at the lowest source locations within the detector cavity, specifically P1 and P2, the geometrical solid angle Ω_G approaches approximately 4π steradians. Conversely, at higher source locations outside the detector cavity, namely P9 and P10, the value of the geometrical solid angle decreases significantly. In fig. 10, the variation of the geometrical solid angle Ω_G was investigated as a function of the location of the radioactive point source, ranging from P1 to P10. Additionally, the influence of photon energy was explored, spanning from 0.05 MeV to 10 MeV.

The total efficiency $\varepsilon_{T(axial)}$ of a *Romashka* NaI(Tl) unit in relation to radioactive sources was evaluated at ten different separation locations, ranging from

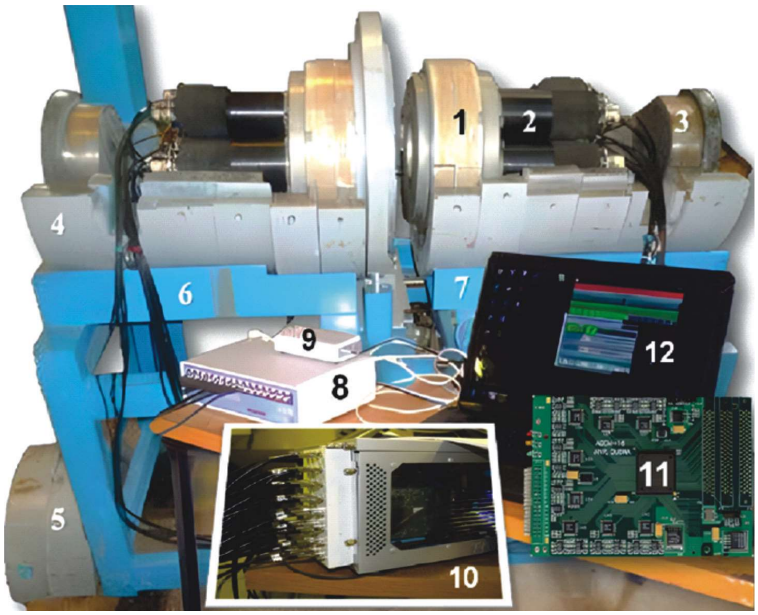

Figure 8. The NaGRaDA main modules, numbered from 1 to 12, are shown in the collage picture and are described in the text.

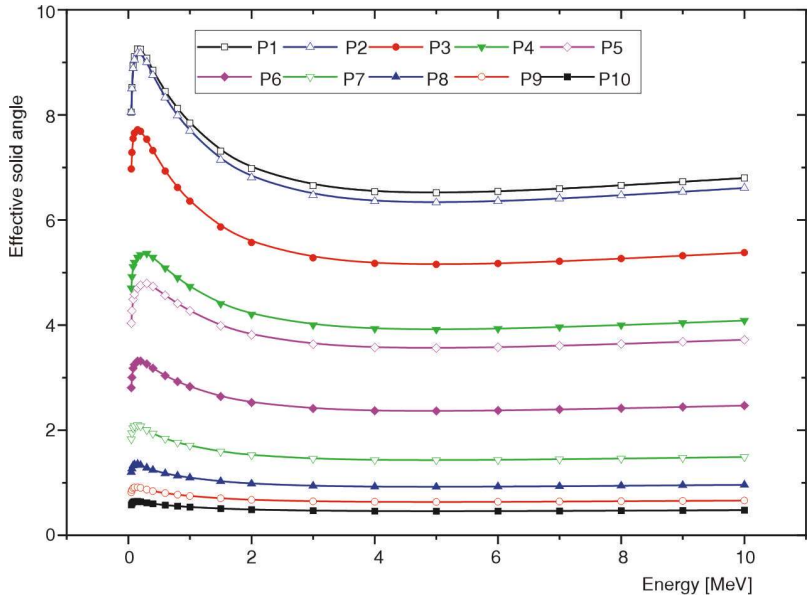

Figure 9. Variation of the effective solid angle as a function of photon energy at positions from P1 to P10

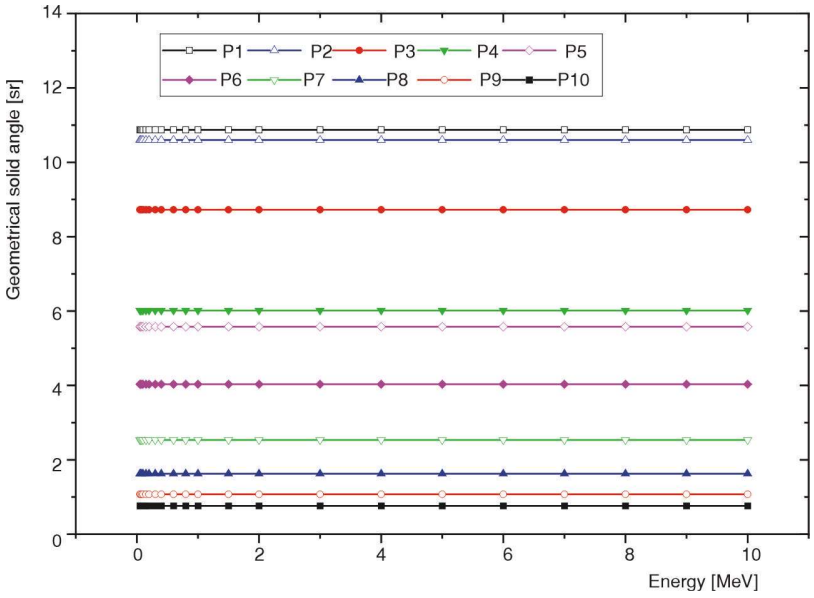

Figure 10. Variation of the geometrical solid angle as a function of photon energy at positions from P1 to P10

Table 1. Total efficiency variation at positions from P1 to P10 as a function of photon energy ranging from 0.05 MeV to 10 MeV

Energy [MeV]	P1	P2	P3	P4	P5	P6	P7	P8	P9	P10
0.05	0.640	0.641	0.555	0.374	0.321	0.224	0.146	0.096	0.065	0.046
0.06	0.678	0.676	0.580	0.391	0.340	0.239	0.155	0.101	0.068	0.048
0.08	0.711	0.707	0.601	0.407	0.357	0.253	0.162	0.106	0.071	0.051
0.1	0.725	0.720	0.609	0.413	0.365	0.259	0.165	0.107	0.073	0.051
0.15	0.736	0.730	0.614	0.421	0.374	0.264	0.167	0.108	0.073	0.051
0.2	0.736	0.730	0.612	0.425	0.379	0.264	0.165	0.106	0.072	0.050
0.3	0.722	0.716	0.600	0.427	0.381	0.259	0.159	0.102	0.069	0.049
0.4	0.704	0.697	0.583	0.421	0.377	0.253	0.154	0.099	0.067	0.048
0.6	0.672	0.663	0.551	0.405	0.363	0.242	0.146	0.095	0.064	0.046
0.8	0.646	0.636	0.527	0.390	0.351	0.233	0.141	0.090	0.062	0.044
1	0.624	0.612	0.506	0.377	0.340	0.225	0.136	0.087	0.060	0.043
1.5	0.582	0.569	0.467	0.351	0.317	0.210	0.127	0.082	0.056	0.040
2	0.555	0.542	0.443	0.335	0.303	0.201	0.121	0.078	0.054	0.039
3	0.529	0.515	0.420	0.318	0.289	0.192	0.116	0.075	0.051	0.037
4	0.520	0.506	0.412	0.313	0.284	0.189	0.114	0.074	0.051	0.037
5	0.519	0.504	0.410	0.312	0.284	0.188	0.114	0.073	0.051	0.037
6	0.521	0.506	0.412	0.313	0.285	0.189	0.114	0.074	0.051	0.037
7	0.525	0.510	0.415	0.315	0.287	0.190	0.115	0.074	0.051	0.037
8	0.530	0.515	0.419	0.318	0.290	0.192	0.116	0.075	0.052	0.037
9	0.535	0.520	0.423	0.322	0.293	0.194	0.117	0.076	0.052	0.038
10	0.541	0.526	0.428	0.325	0.296	0.196	0.119	0.076	0.053	0.038

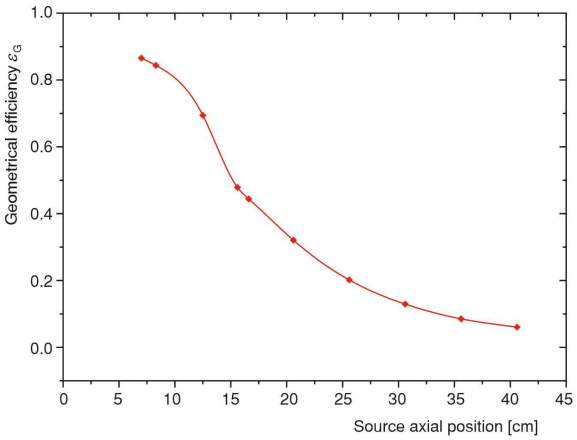

Figure 11. Dependence of geometrical efficiency as a function of the radiation source axial position

P1 to P10. These results are tabulated in tab. 1. The total efficiency $\varepsilon_{T(axial)}$ measured within the energy range of 0.05 MeV to 10 MeV reached its maximum within the detector unit cavity, particularly at position P1. Conversely, while the minimum total efficiency was observed outside it, specifically at position P10.

The variation of the geometrical efficiency denoted as for the *Romashka* NaI(Tl) unit is illustrated in fig. 11. It is evident that geometrical efficiency reaches its maximum when the source is located at the lowest position P1 within the detector cavity. Furthermore, as the source location increases and extends beyond the detector cavity, geometrical efficiency values noticeably decline. This trend highlights the spatial dependence of the detector's performance, necessitating careful consideration of source placement in experimental setups.

Table 2. Average path length at different axial positions

Source axial position $\bar{d}_{(axial)}$	P1	P2	P3	P4	P5	P6	P7	P8	P9	P10
Average path length $\bar{d}_{(axial)}$ [cm]	8.3	8.1	7.8	8.9	8.8	8.3	8.2	8.5	9.0	9.4

In tab. 2 the variation of the average path length $\bar{d}_{(axial)}$ within the *Romashka* NaI(Tl) detector unit was investigated as a function of the radioactive point source location. Given the large volume of the detector, the observed changes in the average path length were minimal. The average path length was determined to be approximately 8.5 cm.

CONCLUSION

The results demonstrate that detection efficiency is significantly affected by both the gamma-rays' source location and energy. These findings hold substantial implications for applications in nuclear physics and radiation detection. They provide valuable insights for manufacturers and researchers regarding the design and optimization of detection structures under specific measurement conditions. Understanding the efficiency and behavior of each detector is crucial before applying quantitative analysis techniques. Apart from the importance of the results, the analytical numerical technique provides a valuable basis for further phenomenological studies of the measurements conducted using these detector arrays.

DATA AVAILABILITY

Access to the data presented in this paper can be provided and for this and any further inquiries about our work please contact the corresponding author.

DECLARATION OF COMPETING INTEREST

The authors confirm that they have no known competitive financial interests or relationships that could be perceived as having influenced the work described in this paper

ORCID NO

A. A. Thabet: 0000-0001-8248-1861
M. S. Badawi: 0000-0002-4919-856X
A. Hamzawy: 0000-0002-9782-8220
I. N. Ruskov: 0000-0002-2084-3211
M. I. Badawi: 0000-0003-0859-8636
I. A. Sirakov: 0000-0002-3421-298X
Y. N. Kopatch: 0000-0003-1688-6996
D. N. Grozdanov: 0000-0002-4268-9307
B. A. Salem: 0000-0003-0811-630X

AUTHORS' CONTRIBUTIONS

This research was conducted within the framework of the international TANGRA Project [24] and involved collaboration among all authors. The contributions are as follows: A. A. Thabet contributed to writing-review and editing (equal), visualization, methodology, and data analysis. A. Hamzawy and B. A. Salem were responsible for writing-original draft preparation, visualization, methodology, and formal analysis. M. I. Badawi and D. N. Grozdanov contributed to writing-review and editing. M. S. Badawi served as project administrator and supervisor, led the Conceptualization, and contributed to writing-review and editing (lead) and validation. I. N. Ruskov was involved in conceptualization, coordination, and writing-review and editing. I. A. Sirakov and Yu. N. Kopatch contributed equally to writing-review and editing.

REFERENCES

[1] Deleanu, D., *et al*., The Gamma Efficiency of the GAINS Spectrometer, *Nuclear Instruments and Methods in Physics Research Section A, 624* (2010), 1, pp. 130-136
[2] Kittel, C., *Introduction to Solid State Physics*, 8th ed. John Wiley & Sons, Inc., 2005, ISBN 0-471-41526-X, https://kaf70.mephi.ru/content/public/uploads/files/pdf/kittel_eng.pdf
[3] Candy, B. H., Photomultiplier Characteristics and Practice Relevant to Photon Counting, *Review of Scientific Instruments, 56* (1985), 2, pp. 183-193
[4] Demir, N., Kuluozturk, Z. N., Determination of Energy Resolution for a NaI(Tl) Detector Modeled with FLUKA Code, *Nuclear Engineering and Technology, 53* (2021), 11, pp. 3759-3763
[5] Luxium, Sodium Iodide Material Data-Sheet. Luxium Solutions, https://www.luxiumsolutions.com/radiation-detection-scintillators/crystal-scintillators/naitl-scintillation-crystals
[6] Knoll, G. F., *Radiation Detection and Measurement*, 4th ed. John Wiley & Sons, Inc., 2010, https://indico-tdli.sjtu.edu.cn/event/171/contributions/2123/attachments/982/1592/Knoll4thEdition.pdf
[7] Badawi, M. S., *et al*., Calibration of 4π NaI(Tl) Detectors with Coincidence Summing Correction Using New Numerical Procedure and ANGLE4 Software, *AIP Advances, 7* (2017), 3, https://doi.org/10.1063/1.4978214
[8] Gouda, M. M., *et al*., Mathematical Method to Calculate Full-Energy Peak Efficiency of Detectors Based on Transfer Technique, *Indian Journal of Physics, 90* (2015), 2, pp. 201-210, https://doi.org/10.1007/s12648-015-0737-1
[9] Abbas, M. I., *et al*., Efficiency of a Cubic NaI(Tl) Detector with Rectangular Cavity Using Standard Radioactive Point Sources Placed at Non-Axial Position, *Applied Radiation and Isotopes, 163* (2020), p. 109139
[10] Abbas, M. I., *et al*., Calibration of a Single Hexagonal NaI(Tl) Detector Using a New Numerical Method Based on the Efficiency Transfer Method, *Nuclear Instruments and Methods in Physics Research Section A, 771* (2015), pp. 110-114
[11] Badawi, M. S., *et al.*, An Empirical Formula to Calculate the Full Energy Peak Efficiency of Scintillation Detectors, *Applied Radiation and Isotopes, 74* (2013), pp. 46-49, https://doi.org/10.1016/j.apradiso.2012.12.011
[12] Badawi, M. S., *et al*., New Algorithm for Studying the Effect of Self Attenuation Factor on the Efficiency of γ-Rays Detectors, *Nuclear Instruments and Methods in Physics Research Section A, 696* (2012), pp. 164-170, https://doi.org/10.1016/j.nima.2012.08.089
[13] Badawi, M. S., *et al*., New Analytical Approach to Calibrate the Co-Axial HPGe Detectors Including Correction for Source Matrix Self-Attenuation, *Applied Radiation and Isotopes, 70* (2012), 12, pp. 2661-2668
[14] El-Khatib, A. M., *et al.*, Well-Type NaI(Tl) Detector Efficiency Using Analytical Technique and ANGLE 4 Software Based on Radioactive Point Sources Located Out the Well Cavity, *Chinese Journal of Physics, 54* (2016), 3, pp. 338-346
[15] Badawi, M. S., A Numerical Simulation Method for Calculation of Linear Attenuation Coefficients of Unidentified Sample Materials in Routine Gamma Ray Spectrometry, *Nuclear Technology and Radiation Protection, 30* (2015), 4, pp. 249-259
[16] Elsafi, M., *et al*., Geant4 Tracks of NaI Cubic Detector Peak Efficiency, Including Coincidence Summing Correction for Rectangular Sources, *Nuclear Science and Engineering, 195* (2021), 9, pp. 1008-1016
[17] El-Khatib, A. M., et al., Computation of the Full Energy Peak Efficiency of an HPGe Detector Using a New Compact Simulation Analytical Approach for Spherical Sources, *Journal of Engineering Science and Technology, 8* (2013), 5, pp. 623-638
[18] Hamzawy, A., *et al*., New Numerical Simulation Method to Calibrate the Regular Hexagonal NaI(Tl) Detector with Radioactive Point Sources Situated

Non-Axial, *Review of Scientific Instruments, 87* (2016), 11, https://doi.org/10.1063/1.4966990
[19] Noureddine, S. F., *et al*., Efficiency Calibration and Coincidence Summing Correction for a NaI(Tl) Spherical Detector, *Nuclear Engineering and Technology, 53* (2021), 10, pp. 3421-3430
[20] Thabet, A. A., Badawi, M. S., Analytical-Numerical Formula for Estimating the Characteristics of a Cylindrical NaI(Tl) Gamma-Ray Detector with a Side--Through Hole, *Nuclear Engineering and Technology, 54* (2022), 10, pp. 3795-3802
[21] Badawi, M. S., Thabet, A. A., Analytical Computation Technique for Calculation the Effective Geometrical Solid Angle and the Efficiency of Cubic Scintillation Crystal with Side Cylindrical Hole, *Nucl Technol Radiat, 37* (2022), 2, pp. 91-102
[22] Harder, J., Material Analysis for Process Control in Cement Plant, *ZKG International, 62* (2009), 6/7, p. 64
[23] Garrett, J. D., Table of Isotopes (Seventh Edition), *Nuclear Physics A, 342* (1980), 3, pp. 528-529
[24] ***, TANGRA Project: Design and Development of the Tagged Neutron Method for Nuclear Reaction Studies and Determination of the Elemental Structure of Substances., Frank Laboratory of Neutron Physics (JINR, Dubna, Russia), n.d., http://flnph.jinr.ru/en/facilities/tangra-project
[25] Niu, D., *et al*., Cross-Section Measurement for (n,2n) Reaction Induced by 14 MeV Neutron on Platinum Isotopes, *Radiation Physics and Chemistry, 177* (2020), 109167 https://doi.org/10.1016/j.radphyschem.2020.109167
[26] Bogolyubov, E. P., *et al.*, Neutron Generators and DAQ Systems for Tagged Neutron Technology, *Proceedings*, XXVI International Symposium on Nuclear Electronics & Computing (NEC'2017), 2017, pp. 176-181 http://ceur-ws.org/Vol-2023/176-181-paper-27.pdf
[27] Dighe, P. M., *et al*., Use of 14 MeV Neutrons in Analysis of Explosive Class Materials, *Journal of Radioanalytical and Nuclear Chemistry, 162* (1992), 2, pp. 277-282
[28] Ruskov, I. N., *et al*., TANGRA-Setup for the Investigation of Nuclear Fission Induced by 14.1 MeV Neutrons, *Physics Procedia, 64* (2015), pp. 163-170 https://doi.org/10.1016/j.phpro.2015.04.022
[29] Ruskov, I. N., *et al*., TANGRA-Setup for the Investigation of Nuclear Fission Induced by 14.1 MeV Neutrons, *Physics Procedia, 64* (2015), pp. 163-170 https://doi.org/10.1016/j.phpro.2015.04.022
[30] Pansare, G. R., Nagesh, N., Bhoraskar, V. N., A Study on Grafting of Acrylonitrile Onto High Density Polyethylene by Neutron Activation, *Journal of Physics D: Applied Physics, 27* (1994), 4, pp. 871-874
[31] Ruskov, I., *et al*., TANGRA – an Experimental Setup for Basic and Applied Nuclear Research by Means of 14.1 MeV Neutrons, *EPJ Web of Conferences, 146* (2017), 03024 https://doi.org/10.1051/epjconf/201714603024
[32] Janeva, N., INRNE Neutron Data Laboratory, BEOBAL Methodological and Coordination Workshop, 22-26 October 2005, Bachinovo, SWU Campus, Blagoevgrad, Bulgaria, n.d., http://www.beo.inrne.bas.bg/BEOBAL/BEOBAL_Presentations/2422_NJ.pdf
[33] Vassilev, N., 4p-Multidetector System Romashka (Daisy). BEOBAL Methodological and Coordination Workshop, 22-26 October 2005, Bachinovo, SWU campus, Blagoevgrad, Bulgaria, n.d., http://www.beo.inrne.bas.bg/BEOBAL/BEOBAL_Presentations/2423_NV.pdf
[34] Mitev, M., *et al.*, Strategy for Sustainable Utilization of IRT-Sofia Research Reactor, Technical Meeting on Commercial Products and Services of Research Reactors (IAEA, Vienna), (2010), n.d., https://www-pub.iaea.org/MTCD/Publications/PDF/SupplementaryMaterials/TECDOC_1713_CD/template-cd/datasets/presentations/15_Bulgaria_Mitev.pdf
[35] Ivanov, I. Z., Activities Concerning the Project on the Small Reactor IRT-200 at Institute for Nuclear Research and Nuclear Energy (INRNE), INPRO Dialogue Forum on Nuclear Energy Innovations, Vienna, Austria, (2011, October 10-14), n.d., https://nucleus.iaea.org/sites/INPRO/df3/Session%202/22.Ivanov-Bulgaria.pdf
[36] Muradyan, G. V., *et al*., Analysis of the Possibilities of the Neutron-Resonance Method of Determining the Elemental Composition of Matter, *Atomic Energy, 109* (2010), 1, pp. 40-45
[37] ***, Frank Laboratory of Neutron Physics, IREN facility. Joint Institute for Nuclear Research, n.d., https://flnp.jinr.int/en-us/main/facilities/iren
[38] Muradyan, G. V., *et al*., Multiplicity Spectrometer for Measuring Neutron Cross Sections, *Nuclear Science and Engineering, 90* (1985), 1, pp. 60-74
[39] ***, AFI Electronics, ADCM-16: 16-Channel 10-bit 100 MHz ADC Board with Signal Processing Core, Joint Institute for Nuclear Research, n.d., https://afi.jinr.ru/ADCM-16
[40] Ruskov, I., *et al.*, Prompt Gamma Emission in Resonance Neutron Induced Fission of ^{239}Pu, *Physics Procedia, 31* (2012), pp. 35-42 https://doi.org/10.1016/j.phpro.2012.04.006
[41] Grozdanov, D. N., Determination of the Dead-Time Losses in NaI(Tl) Gamma-Ray Spectrometer, *Proceedings*, 21st International Seminar on Interaction of Neutrons with Nuclei (ISINN-21), 2013, May 20-25, pp. 176-181, Joint Institute for Nuclear Research, n.d., http://isinn.jinr.ru/proceedings/isinn-21/pdf/grozdanov.pdf
[42] ***, Parsek LLC, 4K Spectrometric ADC with USB Interface and USB Bus Supply, Dubna, Russia, n.d., http://www.parsek.ru/en/products/4KSACPUSB.html

Received on April 30, 2025
Accepted on May 8, 2025

**Абузеид А. ТАБЕТ, Мохамед С. Бадави, Ајман ХАМЗАВИ,
Иван Н. РУСКОВ, Мохамед И. БАДАВИ, Иван А. СИРАКОВ, Јури Н. КОПАЧ,
Димитар Н. ГРОЗДАНОВ, Бохајса А. САЛЕМ**

ДИРЕКТНА АНАЛИТИЧКА ПРОЦЕНА ЕФИКАСНОСТИ NaI(Tl) ДЕТЕКТОРА ГАМА ЗРАКА (*РОМАШКА*)

Рад се фокусира на аналитичке и нумеричке прорачуне просторног угла, ефективног просторног угла, ефикасности и просечне дужине пута гама зрака унутар материјала детектора као функције положаја извора. Анализа је спроведена за модул *Ромашка* 4π NaI(Tl) гама-зрачног детекторског низа (НаГРаДА). НаГРаДА се састоји од 2 × 2π модула детектора гама зрака, при чему се сваки модул састоји од шест NaI(Tl) кристала распоређених у компактној конфигурацији која подсећа на цвет тратинчице (познат као *Ромашка* на руском). Сваки од дванаест сцинтилатора има јединствен дизајн, што их разликује по облику и величини од конвенционалних сцинтилационих детектора. Овај тип 4π мултидетекторског система је применљив за мерење гама зрачења из узорака који показују веома ниску активност. Користи се у анализи активације неутрона и анализи активације брзог гама неутрона. Штавише, овај систем може бити инструментализован у експерименталном истраживању карактеристика нуклеарних реакција изазваних неутронима. Резултати добијени директним аналитичким и нумеричким методама биће упоређени са предстојећом свеобухватном карактеризацијом надограђене и модернизоване *Ромашка* НаГРаДА. Ово поређење користиће GEANT4 симулације поред стандардних тачкастих извора гама зрака.

Кључне речи: 4π мултидетекторски низ, геометријски просторни угао, укупна ефикасност, средња дужина пута